JOURNAL OF SOLID STATE CHEMISTRY 107, 76–92 (1993)

Electron Microscopy of Planar Defects in A15 Nb_3Ge

M. ARITA

College of General Education, Nagoya University, Chikusa-ku, Nagoya, 464 Japan

H.-U. NISSEN

ETH-Zürich, Laboratorium für Festkörperphysik, CH-8093 Zürich, Switzerland

Y. KITANO

Department of Materials Science, Faculty of Science, Hiroshima University, Higashi-Hiroshima, 724 Japan

AND W. SCHAUER

Kernforschungszentrum Karlsruhe, Institut für Technische Physik, D-7500 Karlsruhe, Germany

Received October 16, 1992; in revised form February 23, 1993; accepted February 25, 1993

Planar defects in coevaporated Nb_3Ge films with the A15 structure are investigated by means of high resolution electron microscopy. The defects are usually on {100} and {110}. The high resolution electron micrographs of these defects allow one to deduce the main translation vector; i.e., $(1/2) \cdot \langle 111 \rangle$. The atomic configurations of these defects are investigated by comparing the observed images and the theoretical contrast calculations. There is a good fit between experimental and calculated images for the assumed defect models. © 1993 Academic Press, Inc.

Introduction

The A_3B materials with the A15 structure consist of A-atom chains along three $\langle 100 \rangle$ directions and a bcc sublattice of B atoms (Fig. 1). Their superconducting properties were reported to be mainly related to the A-atom chains (*1*). Therefore, many studies on several kinds of crystal defects disturbing the atom chains have been undertaken. Among such defects, Essmann and Zerweck (*2*) discussed planar defects which interrupt the linear atom chains. The existence of these defects, however, has not yet been experimentally confirmed in detail, since planar defects have only rarely been observed in A15 materials (*3–6*). This work presents the results of a study on planar defects in evaporated Nb_3Ge films by means of high resolution electron microscopy (HREM). A discussion of their atomic configurations is also presented.

In a Nb_3Ge superconductor film with $T_c > 20$ K prepared by the coevaporation method, Kitano *et al.* (*7, 8*) observed regions with a characteristic texture in which small Nb_3Ge grains (generally less than 100 nm in diameter) had a common c axis. The electron diffraction patterns of these regions have a *quasi-twelvefold symmetry*. In this paper, such regions in the texture will be called *QTF-regions*. The grain sizes in QTF-regions are smaller than those within other regions in Nb-Ge films. Planar defects are frequently observed in QTF-regions (*7–11*), while they are rare elsewhere.

2. Experimental Procedures

Nb_3Ge superconductor tapes were prepared by the coevaporation method using

0022-4596/93 $5.00

Copyright © 1993 by Academic Press, Inc.
All rights of reproduction in any form reserved.

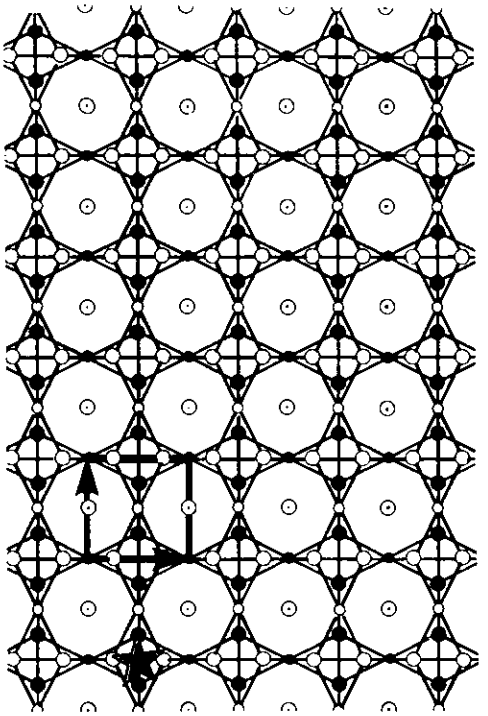

FIG. 1. Structure model of Nb_3Ge (A15) projected onto the (001) plane. Open and closed circles represent atoms at $z = 0$ and $z = \frac{1}{2}$, respectively. The bigger circles are Nb atoms and the smaller circles Ge atoms. Circles with a dot represent two Nb atoms at $z = \pm\frac{1}{4}$ which constitute the Nb chain along the [001] direction. One unit cell is indicated by arrows, whose lattice constant is 0.514 nm. The positions, one of which is indicated by a star, are called the "Tetraederstern" positions in this projection.

pure Nb (MARZ grade, Material Research Corporation) and pure Ge (99.999%, semiconductor purity). The vaporized elements were deposited onto molybdenum polycrystalline substrates (foils with a thickness of 25 μm) kept at about 1.12×10^3 K (≈850°C). The vacuum during the evaporation was in the order of 10^{-6} Pa. The deposition rate was 0.15 to 0.20 nm/sec.

For electron microscopic observations a sample of the film was cut into small pieces, e.g., 1×1 mm^2 in size. These were chemically etched using $FeCl_3$ and HF hydrous solutions, as previously described (*12, 13*). During this procedure, chemical etching in the QTF-regions starts at defects such as small precipitates or grain boundaries.

The etched specimens were investigated in a JEOL JEM 200CX transmission electron microscope operated at 200 kV and equipped with a top entry tilting goniometer (THG-2; ±10° and C_s = 1.2 mm). A LaB_6 cathode was used. The objective aperture used for multibeam HREM images had a diameter of 20 μm. Using this aperture, only the diffraction spots with spatial frequencies smaller than 4.2 nm^{-1} contributed to the image.

3. Defects in the QTF-Regions

Planar defects are frequently observed in the QTF-regions. Typical examples of defects in Nb_3Ge are shown in Fig. 2, the direction of observation for this image is ⟨001⟩. In this projection, defect planes are usually observed on {100} or {110} planes and frequently change their positions and orientations. Throughout this paper, the planar defects on {100} and {110} planes will be termed {100} defects and {110} defects, respectively. The planar defects start and end at grain or phase boundaries, or stop inside a Nb_3Ge grain, introducing partial dislocations (arrow in Fig. 2). Occasionally they occur in the form of a prism so that in the ⟨001⟩ projection a rectangular shape is recognized as indicated by a star in Fig. 2.

In order to determine the translation vectors of planar defects, relative shifts of the white spots caused by such defects were measured in the HREM images observed along ⟨001⟩ (Fig. 3). In Fig. 3a, in which the data for {100} defects are summarized, p and q directions were selected on the image plane so that they were perpendicular respectively parallel to the defect plane. The parameters p and q represent the fractional values of the translation vector (relative to the lattice parameter of the A15 structure). The most common p value is about $\frac{1}{2}$, and the frequent q value of defects with $p = \frac{1}{2}$ is also $\frac{1}{2}$. In addition, examples with $q = 0$ were also observed. In the discussion be-

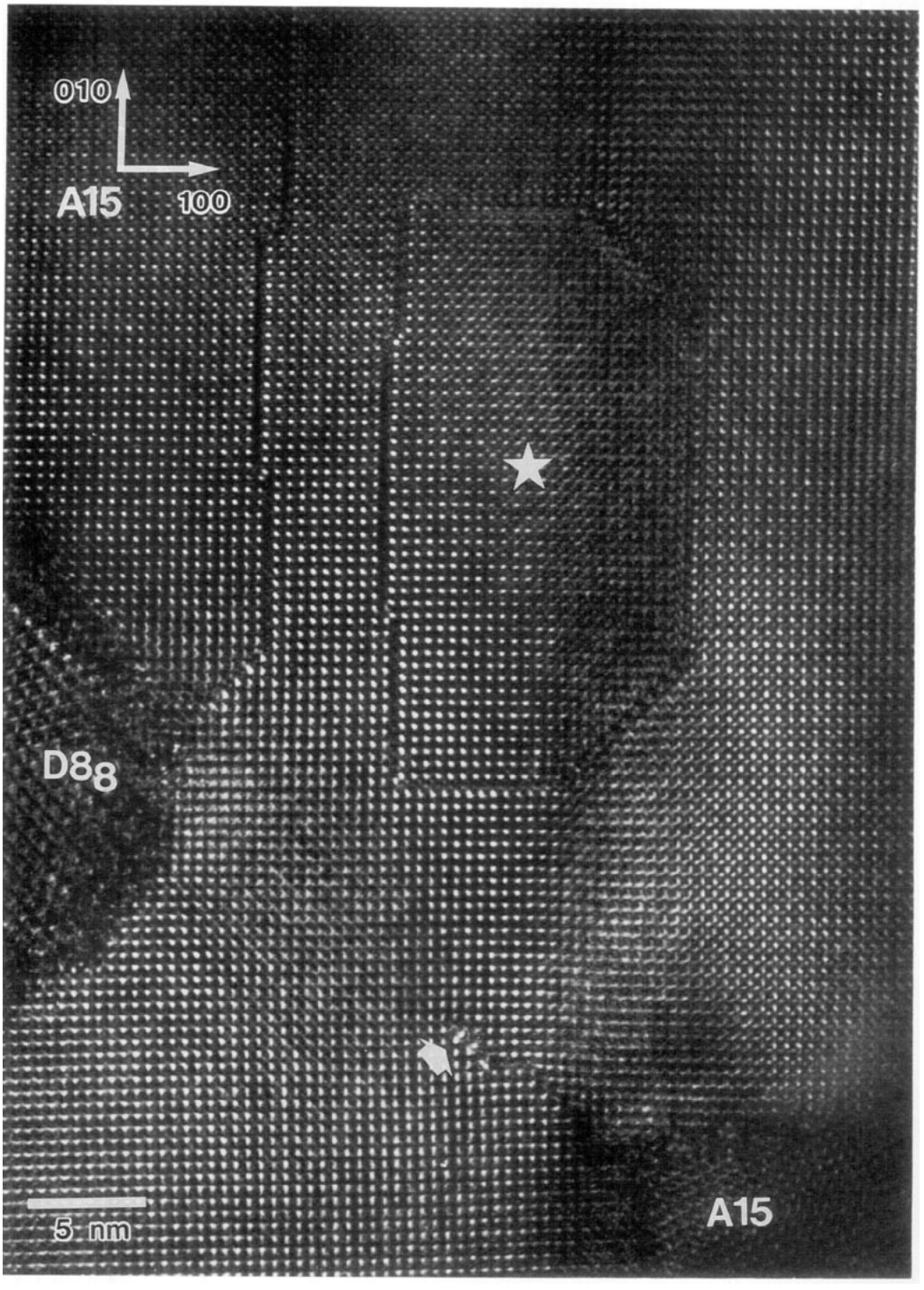

FIG. 2. Example of planar defects in a Nb_3Ge grain observed along ⟨001⟩. The periodicity of the image corresponds to the unit cell. Planar defects start and end at grain or phase boundaries. They also stop inside a grain by introducing a dislocation (arrow). The set of planar defects form a closed loop in the image at the area around a star.

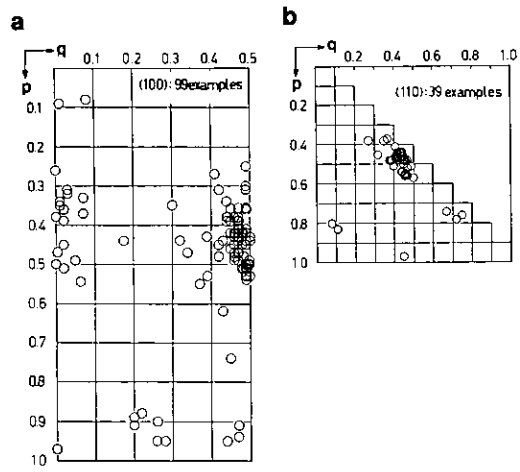

FIG. 3. Projected translation onto the {001} image plane. (a) {100} defects and (b) {110} defects. Each circle indicates one example. Parameters "p" and "q" indicate the fractions of translation relative to the lattice parameter measured along the directions perpendicular and parallel to the defect plane, respectively.

low, only the defects with the values of $[p, q] = [\frac{1}{2}, \frac{1}{2}]$ are treated. If the p direction is fixed to be [100] and thus the defect plane is (100), the q direction should correspond to one of the two directions [010] and [001]. Therefore, the translation vectors $[p, q] = [\frac{1}{2}, \frac{1}{2}]$ mentioned above imply the three dimensional translation vector $[\frac{1}{2}, \frac{1}{2}, r]$ or $[\frac{1}{2}, r, \frac{1}{2}]$, where r is the fractional component in the direction of the incidence. Since it is plausible to assume the HREM observations occur along [010] with equal probability to those occuring along [001], the most probable r value will be $\frac{1}{2}$, however $r = 0$ is also possible. Translation vectors of defects in (100) described above must be $\frac{1}{2} \cdot [111]$ and/or $\frac{1}{2} \cdot [110]$. Figure 3b is the result of defects in (110) projected along [001], where the p and q directions were [100] and [010], respectively. The upper right part of the figure is equivalent to the left part; for example, a point at $p = 0.0$ and $q = 0.2$ corresponds to a point at $p = 0.2$ and $q = 0.0$. The most common value is $[p, q] = [\frac{1}{2}, \frac{1}{2}]$. Since defects with $[p, q] = [\frac{1}{2}, \frac{1}{2}]$ frequently change their defect planes from {110} to {100}, and since for many cases no contrast due to dislocations has been observed at the turning point, the three-dimensional translation vectors of defects in these planes may be the same. Thus the translation vectors of {110} defects in three dimension are probably also $\frac{1}{2} \cdot [111]$ and/or $\frac{1}{2} \cdot [110]$. In addition, it is expected that the atomic arrangements around these two types of defects on {100} and {110} are similar to each other.

A magnified image of one typical planar defect is shown in Fig. 4a observed along [001], where the arrangement of white spots corresponds to the periodicity of the A15 structure. An image of an adjacent hexagonal Nb_5Ge_3 ($D8_8$) precipitation is also shown (Fig. 4b) as well as a laser-optical diffraction pattern from a nearby amorphous contamination region (Fig. 4c). The images in Figs. 4a and 4b were taken from a thicker part of a region showing the second bright thickness fringe where the crystal thickness was estimated as approximately 15–20 nm, and the optical diffraction pattern in Fig. 4c indicates the defocus value of $\Delta f = -130$ nm (underfocus). Sets of image calculations were performed assuming different imaging conditions which have similar values to those mentioned above. The best fit contrasts were given for 19.55 nm thick Nb_3Ge and 15.04 nm thick Nb_5Ge_3 with $\Delta f = -130$ nm, as shown in Fig. 4. Since the chemical etching starts at small precipitates of Nb_5Ge_3, the observed thickness differences in Figs. 4a and 4b appear to be reasonable. In this micrograph, the bright spots correspond to the "Tetraederstern" positions in the A15 structure (Fig. 1) and the Nb-chain positions of Nb_5Ge_3 ($D8_8$) (*14, 15*). Because the defects discussed in the next section were in Fig. 4a or in a region nearby, their contrast calculations will be presented by assuming the imaging condition described above, while the calculated images were checked also under other similar conditions. As indicated above, the defect changes its plane between {110} to {100} without any special arrangement of spots around the de-

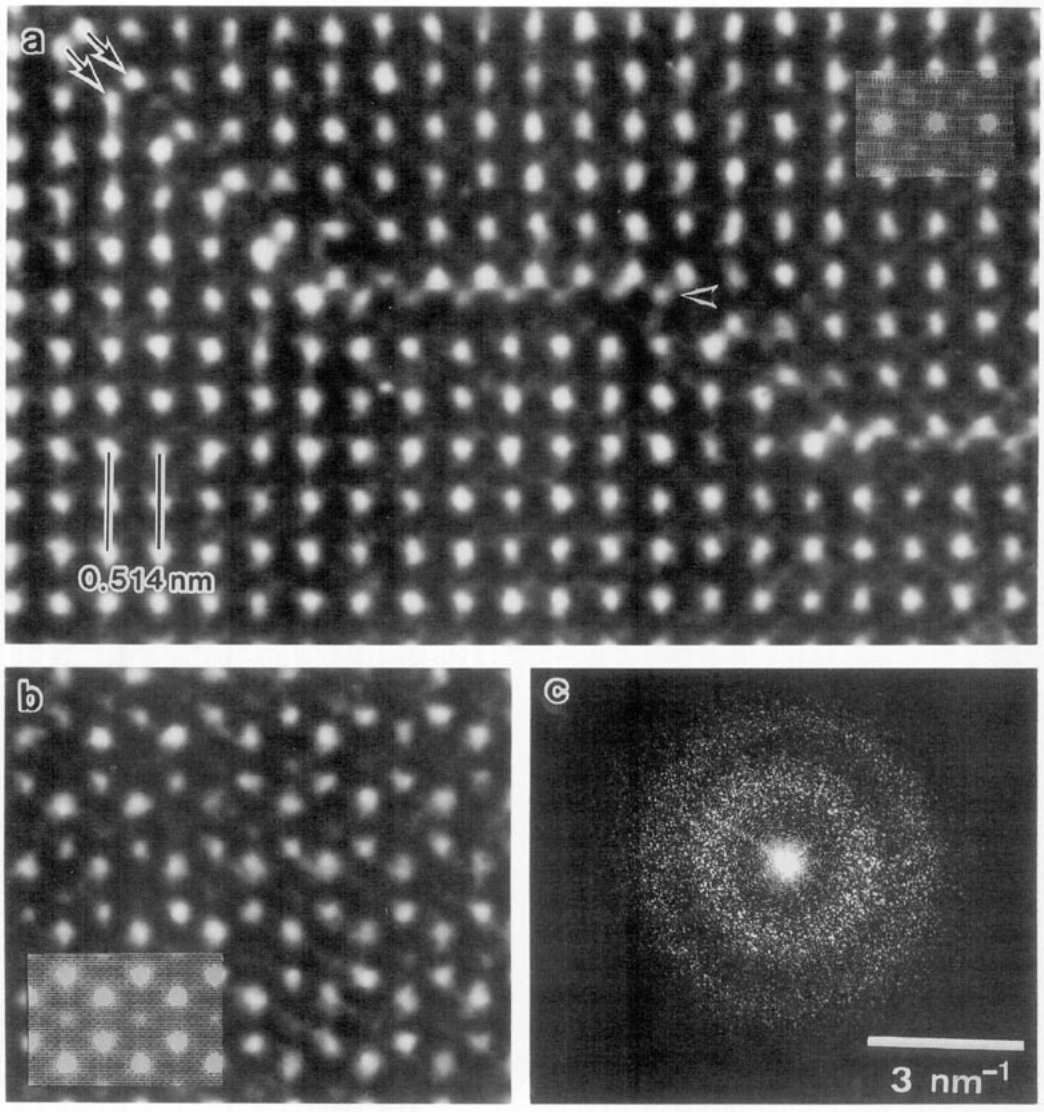

FIG. 4. (a) Typical example of a planar defect. Notice that intensities of the spots about the defect plane are nearly symmetric at both sides of the {110} defect (arrow), while there is an array of weak spots near the {100} defect (arrow head). (b) Structure image of a precipitate of Nb_5Ge_3 near the area shown in (a). (c) Laser optical diffraction pattern of a contaminated area adjacent to the area shown in (a) and (b) indicating $\Delta f = -120$ nm to -140 nm (underfocus). In (a) and (b), the calculated images of Nb_3Ge (thickness: 19.55 nm) and Nb_5Ge_3 (thickness: 15.04 nm) assuming $\Delta f = -130$ nm are inserted.

fect. Near the {110} defect, the arrangement of spots is symmetric (arrows), while there is an array of weak spots (arrow head) at the {100} defect. These characteristic features provide information on the atomic structure of these planar defects.

4. Atomic Configurations of Defects

4.1. {100} Defects

The A15 structure can be described as a stacking structure consisting of three kinds of atomic layers. Three atomic layers α, β,

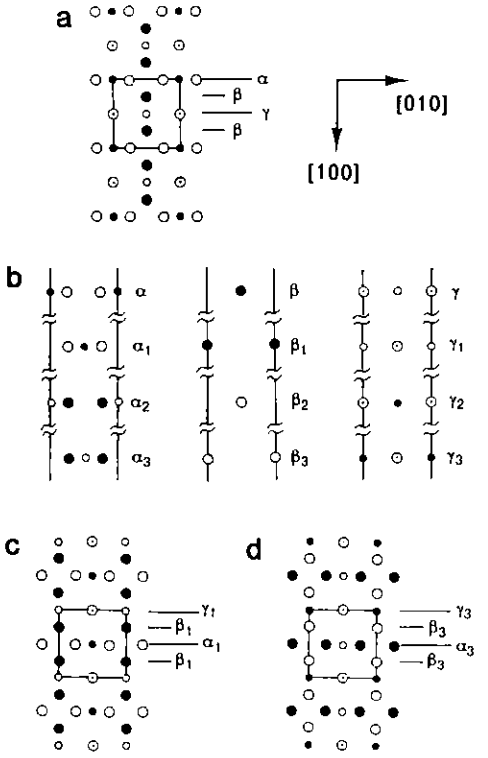

FIG. 5. Stacking sequence along [100] of the A15 structure ([001]-projection). The same symbols as in Fig. 1 are used to interpret the kinds of atoms and the heights along [001]. Unit cells are indicated by squares. (a) The stacking is composed of three types of atom layers on (100), i.e., α, β, and γ. (b) Change in the atom arrangements of the stacking layers α, β, and γ by translations of $\frac{1}{2} \cdot [010]$ (α_1, β_1, and γ_1), $\frac{1}{2} \cdot [001]$ (α_2, β_2, and γ_2) and $\frac{1}{2} \cdot [011]$ (α_3, β_3, and γ_3). Lines mean neighboring (010) planes which constitute the unit cell drawn in (a). (c) and (d) Pattern change of the stacking by translations of $\frac{1}{2} \cdot [110]$ and $\frac{1}{2} \cdot [111]$ relative to (a), respectively; or in other words relative to the unit cell.

and γ are defined in Fig. 5a where the atomic configuration is shown superimposed onto the (001) plane. An α layer consists of Nb atoms at $z = 0$ forming a chain along [010] and Ge atoms at $z = \frac{1}{2}$, a β layer contains Nb atoms at $z = \frac{1}{2}$, and a γ layer Nb atoms at $z = \pm\frac{1}{4}$ forming a chain along [001] and Ge atoms at $z = 0$. Using these symbols, the stacking sequence along [100] is $\ldots\alpha\beta\gamma\beta\ldots$. Translating an α layer in the (100) plane by $\frac{1}{2} \cdot [010]$, $\frac{1}{2} \cdot [001]$, and $\frac{1}{2} \cdot [011]$, the pattern of atom layers is changed into α_1, α_2, and α_3, respectively (Fig. 5b). The similar translation of a β layer and a γ layer gives β_1, β_2, and β_3, and γ_1, γ_2, and γ_3 of Fig. 5b. Here the subscript numbers 1, 2, and 3 denote the layers after the translation of $\frac{1}{2} \cdot [010]$, $\frac{1}{2} \cdot [001]$ and $\frac{1}{2} \cdot [011]$, respectively. Translation of an α layer along the stacking direction by $\frac{1}{2} \cdot [100]$ results in a change from α to γ or from γ to α for any numbers of the subscript. In this case a translation of a β layer by $\frac{1}{2} \cdot [100]$ gives the same β layer. The relations existing, when different layers are combined by the translations considered above, are summarized in Tables Ia and Ib. In Figs. 5c and 5d, the atoms are translated by $\frac{1}{2} \cdot [110]$ and $\frac{1}{2} \cdot [111]$ relative to Fig. 5a. During these processes the unit cell shown in Fig. 5a is not moved. The stacking sequence of atom layers in the unit cell changes to $\ldots\gamma_1\beta_1\alpha_1\beta_1\ldots$ by a translation of $\frac{1}{2} \cdot [110]$. Since $\frac{1}{2} \cdot [110]$ is equal to $\frac{1}{2} \cdot [100] + \frac{1}{2} \cdot [010]$, this change is divided into two parts. As described above, the translation of $\frac{1}{2} \cdot [100]$ gives the change from α to γ and vice versa, and $\frac{1}{2} \cdot [010]$ induces the change, for example, from α to α_1. Similarly a translation of $\frac{1}{2} \cdot [111]$ gives $\ldots\gamma_3\beta_3\alpha_3\beta_3\ldots$. The pattern in Fig. 5d is obtained also by observing Fig. 5a along [010]; in other words the observation along [010] corresponds to a $\frac{1}{2} \cdot [111]$ translation. Combining the information from Figs. 5a, 5c, and 5d, atomic models of defects on (100) with translation vectors of $\frac{1}{2} \cdot [110]$ and $\frac{1}{2} \cdot [111]$ will be constructed in the next paragraph.

The HREM images do not reveal any special structure around the defect region. Therefore the defect model will be made by simply combining two of these three figures. For example, in the case of the defect with $\frac{1}{2} \cdot [110]$, Fig. 5a is cut between the layers α and β, and Fig. 5c between γ_1 and β_1. Connecting the upper part of Fig. 5a with the lower part of Fig. 5c, the stacking of layers around the defect plane is

$$\ldots\beta\gamma\beta[\alpha\beta\gamma\beta]\alpha/\beta_1\alpha_1\beta_1[\gamma_1\beta_1\alpha_1\beta_1]\gamma_1\ldots\,, \quad (1)$$

where the slash means the boundary plane and the brackets are unit cells in Figs. 5a and 5c. This structure model can be considered as a stacking fault. Other possibilities for cutting positions are between β and γ, γ and β, and β and α for Fig. 5a. The corresponding positions for Fig. 5c are between β_1 and α_1, α_1 and β_1, and β_1 and γ_1, respectively. The resulting stacking sequences are

$$\ldots\gamma\beta[\alpha\beta\gamma\beta]\alpha\beta/\alpha_1\beta_1[\gamma_1\beta_1\alpha_1\beta_1]\gamma_1\beta_1\ldots \quad (2)$$
$$\ldots\beta[\alpha\beta\gamma\beta]\alpha\beta\gamma/\beta_1[\gamma_1\beta_1\alpha_1\beta_1]\gamma_1\beta_1\alpha_1\ldots \quad (3)$$
$$\ldots[\alpha\beta\gamma\beta]\alpha\beta\gamma\beta/[\gamma_1\beta_1\alpha_1\beta_1]\gamma_1\beta_1\alpha_1\beta_1\ldots\ . \quad (4)$$

Among the four stacking models, (1) and (2) result in the same structure. Exchanging the right and the left parts of model (2), the stacking becomes

$$\ldots\beta_1\gamma_1[\beta_1\alpha_1\beta_1\gamma_1\beta_1]\alpha_1/\beta\alpha[\beta\gamma\beta\alpha]\beta\gamma\ldots\ .$$

A translation of the whole structure by $\frac{1}{2}\cdot$ [010] induces changes, for example, from α to α_1 and α_1 to α. Thus the stacking sequence is

$$\ldots\beta\gamma\beta\alpha\beta\gamma\beta\alpha/\beta_1\alpha_1\beta_1\gamma_1\beta_1\alpha_1\beta_1\gamma_1\ldots\ .$$

This is exactly equal to the stacking sequence (1). In the same way, it is proved that (3) and (4) are identical. In summary, there are only two possible arrangements for the defect on (100) with $\frac{1}{2}\cdot$ [110]. In Figs. 6a and 6b, structure models for the stackings (1) and (4) are presented. In the model (1), the distance between a Ge atom in the α layer (small full circle) and a Nb atom in the β_1 layer (large full circle) is short, i.e., 0.129 nm. Therefore a model without these Nb atoms (Fig. 6a) and one without these Ge atoms (Fig. 6a′) are presented.

In a similar procedure, models for defects with $\frac{1}{2}\cdot$ [111] are obtained using Figs. 5a and 5d. In this case, there are also two possible patterns in the projection along [001]:

$$\ldots\beta\gamma\beta[\alpha\beta\gamma\beta]\alpha/\beta_3\alpha_3\beta_3[\gamma_3\beta_3\alpha_3\beta_3]\gamma_3\ldots \quad (5)$$

and

$$\ldots[\alpha\beta\gamma\beta]\alpha\beta\gamma\beta/\gamma_3\beta_3\alpha_3\beta_3[\gamma_3\beta_3\alpha_3\beta_3]\ldots\ . \quad (6)$$

Figures 6c and 6d are structure models for the stackings (5) and (6), respectively. Actually, stacking models (5) and (6) are identical in three dimensions. Observation of model (5) along the [010] direction causes the following change, since the projection along [010] is consistent with a translation $\frac{1}{2}\cdot$ [111] in three dimensions:

$$\ldots\beta_3\alpha_3\beta_3\gamma_3\beta_3\alpha_3\beta_3\gamma_3/\beta\gamma\beta\alpha\beta\gamma\beta\alpha\ldots\ .$$

Exchange of the left and the right parts gives the following stacking sequence:

$$\ldots\alpha\beta\gamma\beta\alpha\beta\gamma\beta/\gamma_3\beta_3\alpha_3\beta_3\gamma_3\beta_3\alpha_3\beta_3\ldots$$

This is exactly the stacking model (6). In summary, there is only one defect structure for the defect with $\frac{1}{2}\cdot$ [111], and there are two types of projected patterns along [001]. Since the analyses are performed using the HREM images observed along [001], these two projected patterns should be treated as different cases in the following discussion.

As elaborated above, five projection models onto the (001) plane were obtained for the {100} defect. Comparing the observed HREM contrast with the theoretically calculated images, the best model can be determined. The program for the calculation is EMSYS (*16*) modified by one of the present authors (*11*). Results of such image calculations based on the multislice method are summarized in Fig. 7 for the defect models shown in Fig. 6. Among the five calculated images, the characteristic features in the observed image consisting an array of weak spots at the defect plane appears in Fig. 7c only. This case corresponds to the stacking model (5), with the translation of $\frac{1}{2}\cdot$ [111].

4.2. {110} Defects

Along the [110] direction, the A15 structure also has a stacking of three kinds of atom layers, i.e., δ, ε, and ζ in Fig. 8a. The δ layer contains a Nb chain along [001] at $z = \pm\frac{1}{4}$, the ε-layer Nb atoms at $z = 0$ and $\frac{1}{2}$, and the ζ-layer Ge atoms at $z = 0$ and $\frac{1}{2}$. Translation of atoms relative to the square unit induces the change of the atom layers.

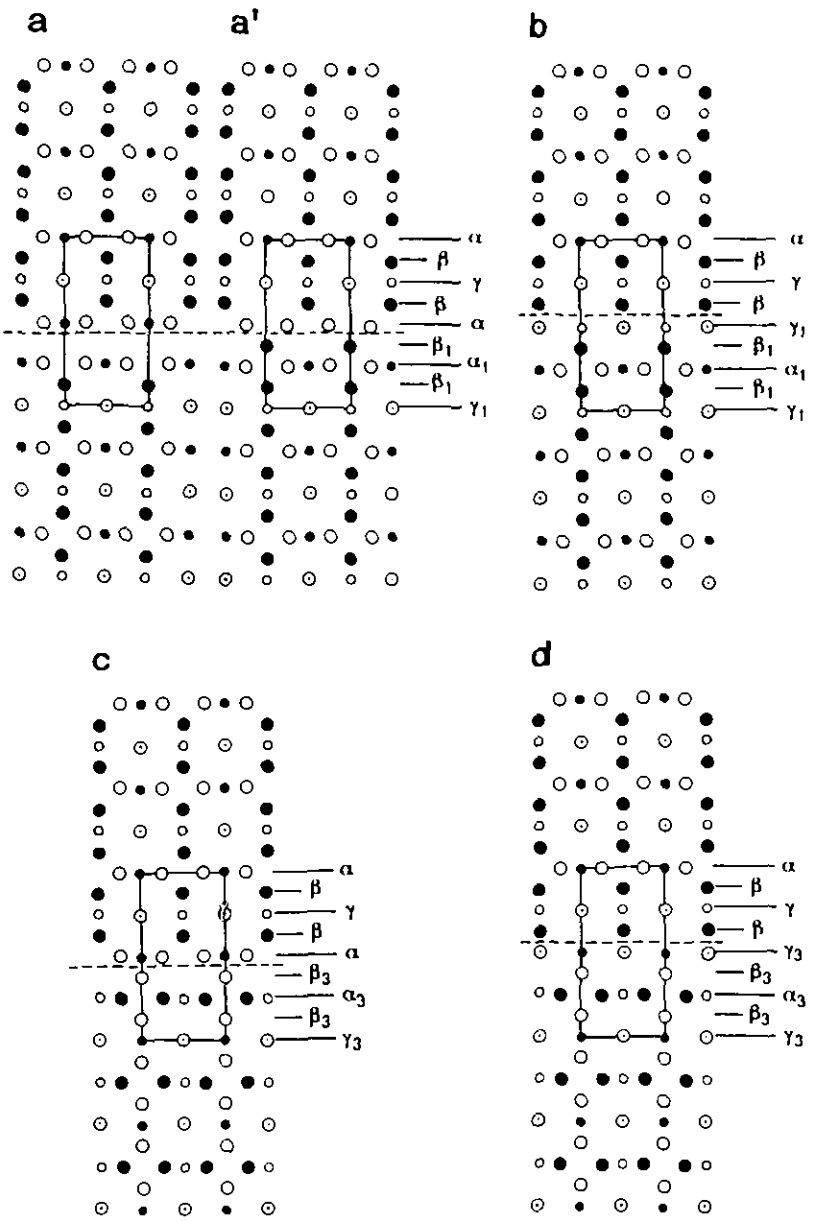

FIG. 6. Possible structure models for the defect in (100) with translations of (a), (a'), and (b) $\frac{1}{2} \cdot [110]$, and (c) and (d) $\frac{1}{2} \cdot [111]$. Positions of the defect planes are marked by broken lines. Stacking sequences in the regions near the defect planes (indicated by rectangles) are shown. The corresponding layer sequences described in the text are the stacking (1) for (a) and (a'), the stacking (4) for (b), the stacking (5) for (c) and the stacking (6) for (d). When the interatomic distances at the boundary region are short, these atoms are omitted as shown in (a) and (a').

For the {110} defect, the elemental translations within the defect plane (110) are $\frac{1}{2} \cdot [1\bar{1}0]$ and $\frac{1}{2} \cdot [001]$, and the one perpendicular to the (110) plane is $\frac{1}{2} \cdot [110]$. In this case, the translation $\frac{1}{2} \cdot [1\bar{1}0]$ in the defect plane gives the same change as introduced by $\frac{1}{2} \cdot [110]$ perpendicular to the defect. In Fig. 8b, the change of atom positions in the stacking

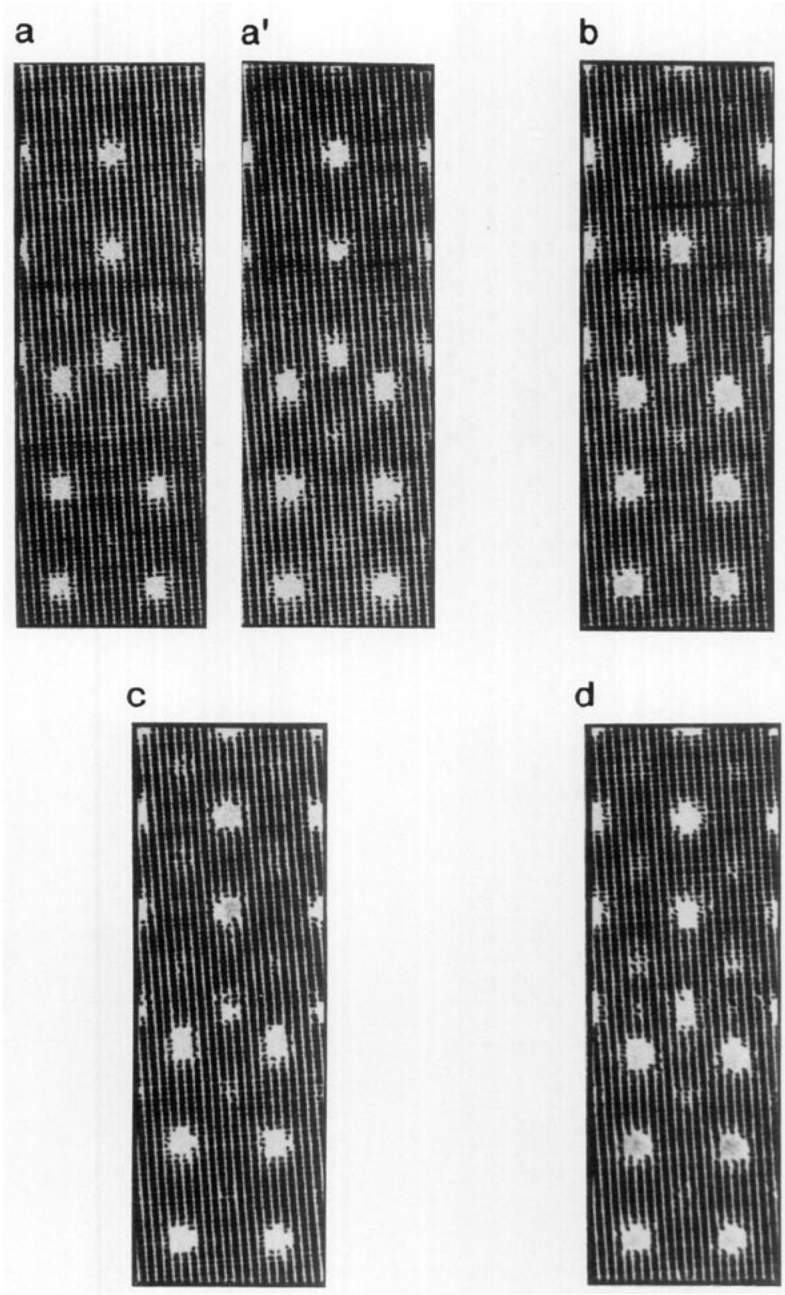

FIG. 7. Calculated images of the defect models shown in Fig. 6 based on the multislice method. Notation such as (a) and (a′) is the same as in Fig. 6. Crystal thickness of 19.55 nm and a defocus value of −130 nm (underfocus) are assumed. The most probable image which fits to the observation is (c).

planes are presented, which are obtained by the translation of $\frac{1}{2} \cdot [110]$, $\frac{1}{2} \cdot [001]$, and $\frac{1}{2} \cdot [111]$. They are designated by subscripts 1, 2 and 3, respectively. It is clearly recognized that $\delta_2 = \delta$, $\delta_3 = \delta_1$, $\zeta_2 = \zeta_1$, and $\zeta_3 = \zeta$. The relations among the layers resulting from these translations are summarized in Table Ic. Based on this notation, the

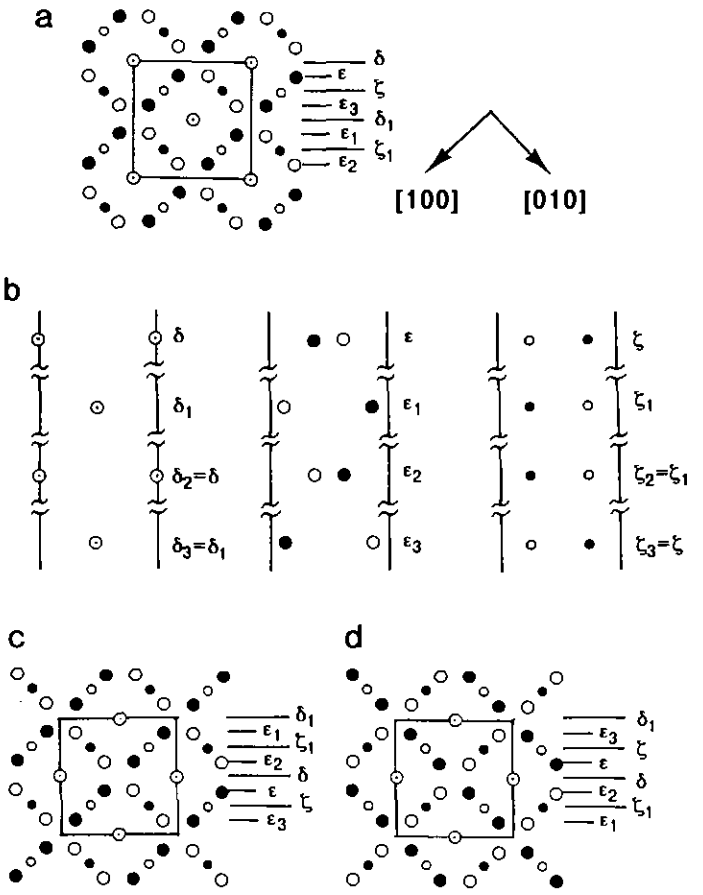

FIG. 8. Stacking sequences along [110] of the A15 structure ([001] projection). Meanings of the symbols used in the figures are the same as in Fig. 1. Smallest unit along [110] is drawn by a square which has eight {110} planes. (a) The stacking is composed of three types of atom layers on (110), i.e., δ, ε, and ζ. (b) Change in the atom arrangements of the stacking layers δ, ε, and ζ by translations of $\frac{1}{2}\cdot[110]$ (δ_1, ε_1, and ζ_1), $\frac{1}{2}\cdot[001]$ (δ_2, ε_2, and ζ_2) and $\frac{1}{2}\cdot[111]$ (δ_3, ε_3, and ζ_3). Note $\delta_2=\delta$, $\delta_3=\delta_1$, $\zeta_2=\zeta_1$, and $\zeta_3=\zeta$. Lines indicate two $(1\bar{1}0)$ planes which construct the square unit in (a). (c) and (d) Pattern change of the stacking by translations of $\frac{1}{2}\cdot[110]$ and $\frac{1}{2}\cdot[111]$ relative to (a).

stacking sequence along [110] is $\ldots\delta\varepsilon\zeta\varepsilon_3\delta_1\varepsilon_1\zeta_1\varepsilon_2\ldots$. In Figs. 8c and 8d, the atoms are translated relative to Fig. 8a by $\frac{1}{2}\cdot[110]$ and $\frac{1}{2}\cdot[111]$, respectively. Here the position of the square unit is unchanged. By these treatments the stacking sequences in the square unit are changed to $\ldots\delta_1\varepsilon_1\zeta_1\varepsilon_2\delta\varepsilon\zeta\varepsilon_3\ldots$ and $\ldots\delta_1\varepsilon_3\zeta\varepsilon\delta\varepsilon_2\zeta_1\varepsilon_1\ldots$, respectively. As for the defect in (100), the structure models of defect in (110) are made by simply cutting and joining together in the appropriate way, Figs. 8a, 8c, and 8d.

There are eight possibilities to cut the square unit in Fig. 8a, e.g. between δ and ε, ε and ζ, ζ and ε_3, ε_3 and δ_1, etc. Correspondingly, the cutting positions in Fig. 8c are between δ_1 and ε_1, ε_1 and ζ_1, ζ_1 and ε_2, ε_2 and δ, etc., respectively. The resulting sequences of layers at the boundary region for the defect with $\frac{1}{2}\cdot[110]$ are

$$\ldots\varepsilon\zeta\varepsilon_3\delta_1\varepsilon_1\zeta_1\varepsilon_2[\delta\varepsilon\zeta\varepsilon_3\delta_1\varepsilon_1\zeta_1\varepsilon_2]\delta/\varepsilon_1\zeta_1\varepsilon_2\delta\varepsilon\zeta\varepsilon_3[\delta_1\varepsilon_1\zeta_1\varepsilon_2\delta\varepsilon\zeta\varepsilon_3]\delta_1\ldots \quad (7)$$

$$\ldots\zeta\varepsilon_3\delta_1\varepsilon_1\zeta_1\varepsilon_2[\delta\varepsilon\zeta\varepsilon_3\delta_1\varepsilon_1\zeta_1\varepsilon_2]\delta\varepsilon/\zeta_1\varepsilon_2\delta\varepsilon\zeta\varepsilon_3[\delta_1\varepsilon_1\zeta_1\varepsilon_2\delta\varepsilon\zeta\varepsilon_3]\delta_1\varepsilon_1\ldots \quad (8)$$

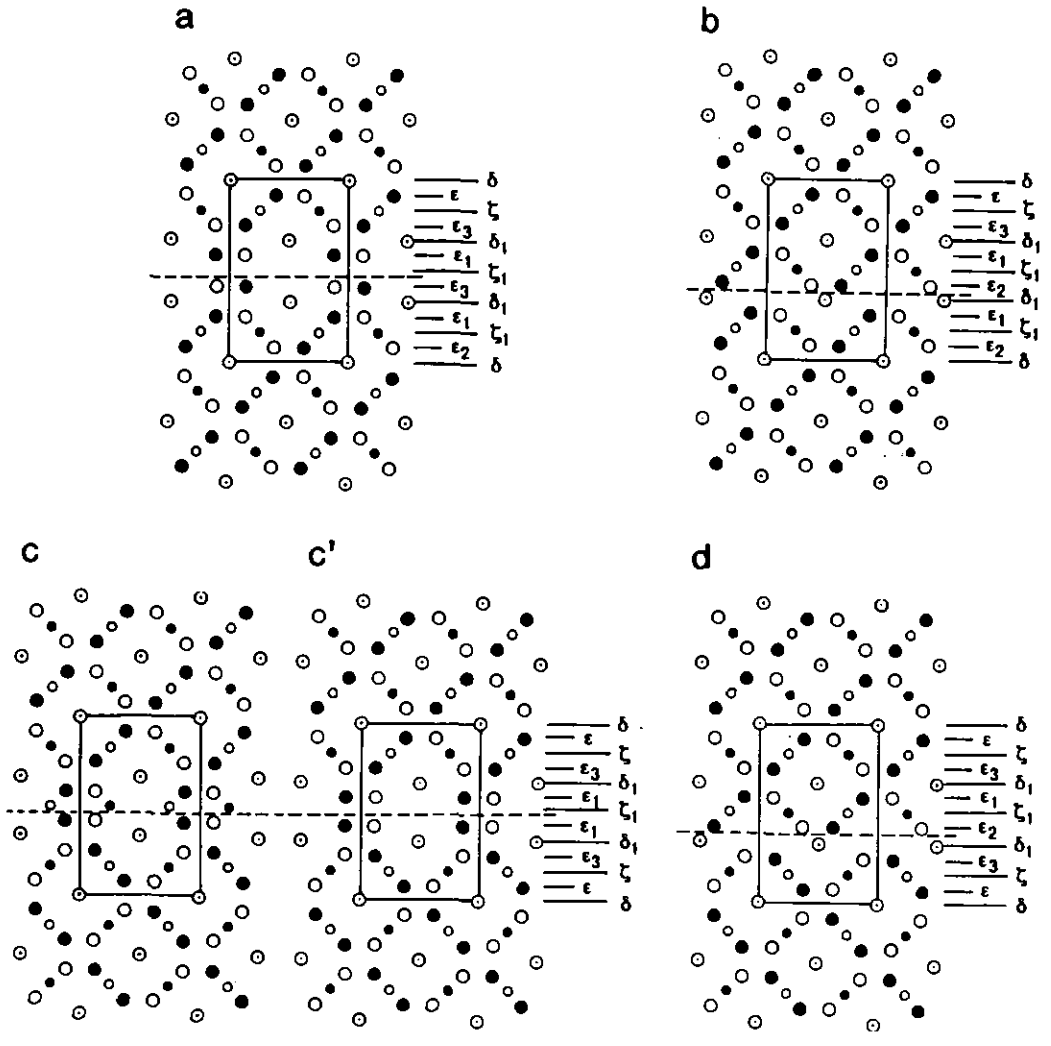

FIG. 9. Possible structure models for the planar defect on (110) with translations of (a) and (b) $\frac{1}{2}\cdot[110]$ and (c), (c'), and (d) $\frac{1}{2}\cdot[111]$. Positions of the defect plane are marked by broken lines. The stacking sequences in the regions near the defect planes (indicated by rectangles) are shown. The model (c') is produced by omitting Ge atoms at the defect plane from the model (c).

$$\ldots\varepsilon_3\delta_1\varepsilon_1\zeta_1\varepsilon_2[\delta\varepsilon\zeta\varepsilon_3\delta_1\varepsilon_1\zeta_1\varepsilon_2]\delta\varepsilon\zeta/\varepsilon_2\delta\varepsilon\zeta\varepsilon_3[\delta_1\varepsilon_1\zeta_1\varepsilon_2\delta\varepsilon\zeta\varepsilon_3]\delta_1\varepsilon_1\zeta_1\ldots \quad (9)$$

$$\ldots\delta_1\varepsilon_1\zeta_1\varepsilon_2[\delta\varepsilon\zeta\varepsilon_3\delta_1\varepsilon_1\zeta_1\varepsilon_2]\delta\varepsilon\zeta\varepsilon_3/\delta\varepsilon\zeta\varepsilon_3[\delta_1\varepsilon_1\zeta_1\varepsilon_2\delta\varepsilon\zeta\varepsilon_3]\delta_1\varepsilon_1\zeta_1\varepsilon_2\ldots \quad (10)$$

$$\ldots\varepsilon_1\zeta_1\varepsilon_2[\delta\varepsilon\zeta\varepsilon_3\delta_1\varepsilon_1\zeta_1\varepsilon_2]\delta\varepsilon\zeta\varepsilon_3\delta_1/\varepsilon\zeta\varepsilon_3[\delta_1\varepsilon_1\zeta_1\varepsilon_2\delta\varepsilon\zeta\varepsilon_3]\delta_1\varepsilon_1\zeta_1\varepsilon_2\delta\ldots \quad (11)$$

$$\ldots\zeta_1\varepsilon_2[\delta\varepsilon\zeta\varepsilon_3\delta_1\varepsilon_1\zeta_1\varepsilon_2]\delta\varepsilon\zeta\varepsilon_3\delta_1\varepsilon_1/\zeta\varepsilon_3[\delta_1\varepsilon_1\zeta_1\varepsilon_2\delta\varepsilon\zeta\varepsilon_3]\delta_1\varepsilon_1\zeta_1\varepsilon_2\delta\varepsilon\ldots \quad (12)$$

$$\ldots\varepsilon_2[\delta\varepsilon\zeta\varepsilon_3\delta_1\varepsilon_1\zeta_1\varepsilon_2]\delta\varepsilon\zeta\varepsilon_3\delta_1\varepsilon_1\zeta_1/\varepsilon_3[\delta_1\varepsilon_1\zeta_1\varepsilon_2\delta\varepsilon\zeta\varepsilon_3]\delta_1\varepsilon_1\zeta_1\varepsilon_2\delta\varepsilon\zeta\ldots \quad (13)$$

$$\ldots[\delta\varepsilon\zeta\varepsilon_3\delta_1\varepsilon_1\zeta_1\varepsilon_2]\delta\varepsilon\zeta\varepsilon_3\delta_1\varepsilon_1\zeta_1\varepsilon_2/[\delta_1\varepsilon_1\zeta_1\varepsilon_2\delta\varepsilon\zeta\varepsilon_3]\delta_1\varepsilon_1\zeta_1\varepsilon_2\delta\varepsilon\zeta\varepsilon_3\ldots . \quad (14)$$

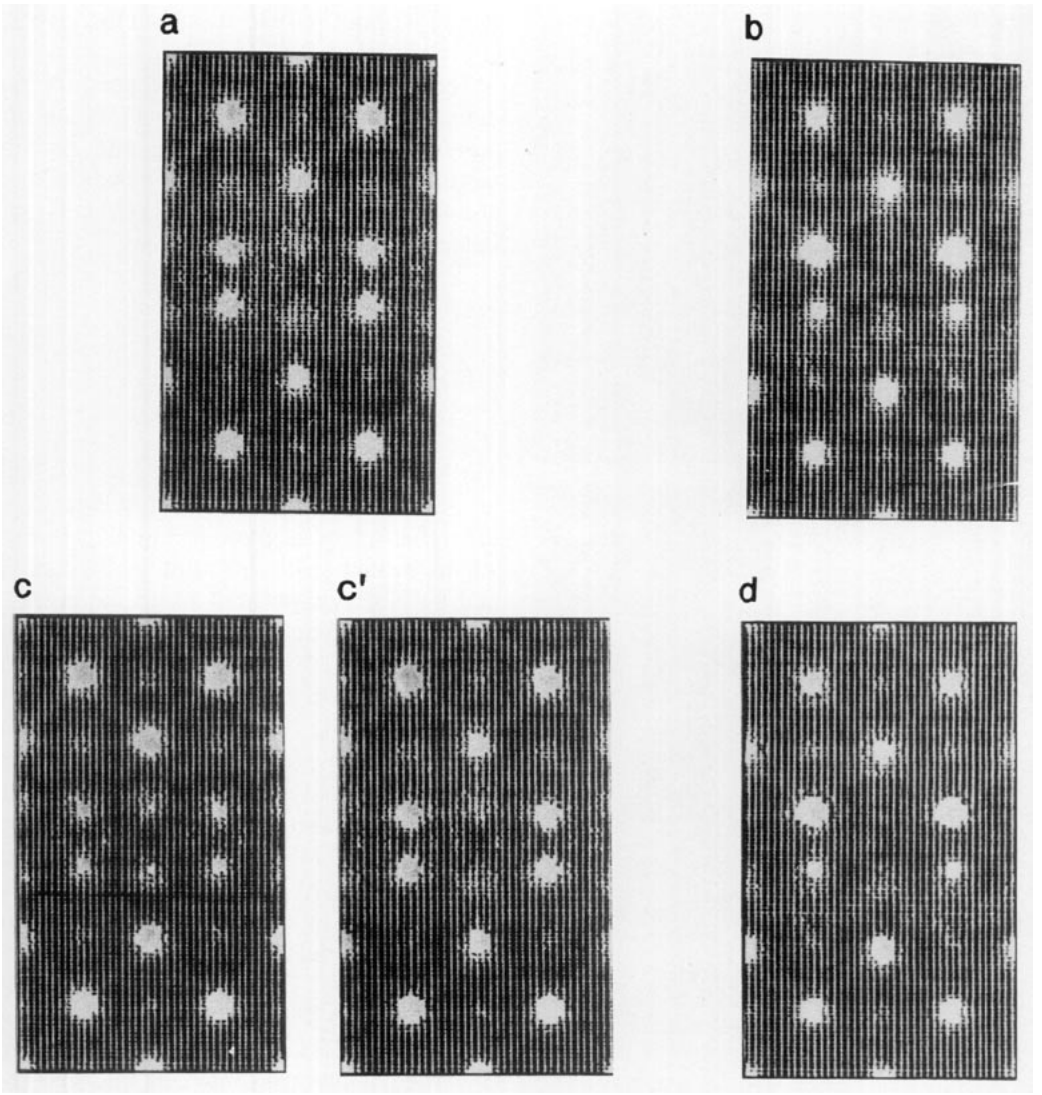

FIG. 10. Calculated images of the defect models presented in Fig. 9 based on the multislice method. Notation of the figures such as (a) and (b) are the same as in Fig. 9. Crystal thickness of 19.55 nm and a defocus value of −130 nm (underfocus) are assumed. The best image to fit the observation is (c').

Here the brackets indicate the stacking units along [110] in Fig. 8. The stacking model (7) is converted into the models (10), (11) and (14) by the following processes:

- By the exchange of the right and the left parts, the stacking becomes

$$\ldots\delta_1\varepsilon_3\zeta\varepsilon\delta\varepsilon_2\zeta_1\varepsilon_1\delta_1\varepsilon_3\zeta\varepsilon\delta\varepsilon_2\zeta_1\varepsilon_1/$$
$$\delta\varepsilon_2\zeta_1\varepsilon_1\delta_1\varepsilon_3\zeta\varepsilon\delta\varepsilon_2\zeta_1\varepsilon_1\delta_1\varepsilon_3\zeta\varepsilon\ldots .$$

Further, the translation of the whole pattern by $\frac{1}{2}\cdot[001]$ gives

$$\ldots\delta_1\varepsilon_1\zeta_1\varepsilon_2\delta\varepsilon\zeta\varepsilon_3\delta_1\varepsilon_1\zeta_1\varepsilon_2\delta\varepsilon\zeta\varepsilon_3/$$
$$\delta\varepsilon\zeta\varepsilon_3\delta_1\varepsilon_1\zeta_1\varepsilon_2\delta\varepsilon\zeta\varepsilon_3\delta_1\varepsilon_1\zeta_1\varepsilon_2\ldots$$

since this translation induces the exchange of the layer patterns between ε and ε_2, ε_1 and ε_3, and ζ and ζ_1, respectively. Note δ and δ_1 remain unchanged. This stacking is exactly the stacking model (10).

- The translation of the whole pattern by $\frac{1}{2}\cdot[110]$ produces the model (11).

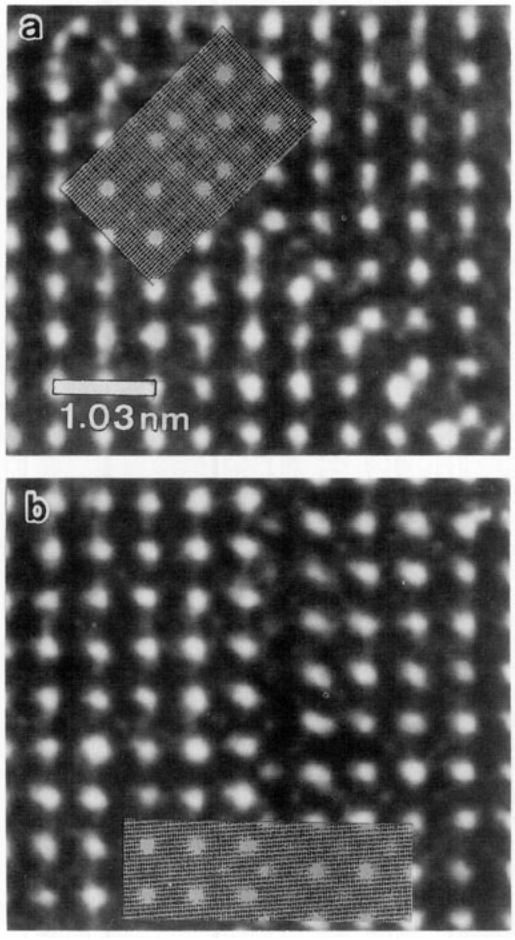

FIG. 11. Electron micrographs of defects on (a) (110) and (b) (100) with $[\frac{1}{2}\ \frac{1}{2}]$ translation in the image plane. The observed images are compared with the calculated images, Figs. 7c and 10c'.

• Exchange of the right and left parts and the translation by $\frac{1}{2} \cdot [111]$ gives model (14).

In the same way it is recognized that models (8), (9), (12) and (13) are identical. In summary, there are two stacking sequences for the defect in (110) with a translation vector $\frac{1}{2} \cdot [110]$, i.e., (13) and (14). Figures 9a and 9b are representations of the models (13) and (14), respectively. In the stacking model (13), interatomic distances are short at the boundary plane, i.e., between Ge atoms on the layer ζ_1 and Nb atoms on the layer ε_3 (0.129 nm). Thus in the drawing, only the model without the Ge atoms on the layer ζ_1 is presented in Fig. 9a.

The possible stacking sequences for the defect with the translation $\frac{1}{2} \cdot [111]$ are obtained by using the cutting and pasting method for Figs. 8a and 8d as described just above. In this case, there are also only two independent stacking sequences:

$$\ldots\varepsilon_2[\delta\varepsilon\zeta\varepsilon_3\delta_1\varepsilon_1\zeta_1\varepsilon_2]\delta\varepsilon\zeta\varepsilon_3\delta_1\varepsilon_1\zeta_1/\varepsilon_1[\delta_1\varepsilon_3\zeta\varepsilon\delta\varepsilon_2\zeta_1\varepsilon_1]\delta_1\varepsilon_3\zeta\varepsilon\delta\varepsilon_2\zeta_1\ldots \quad (15)$$

$$\ldots[\delta\varepsilon\zeta\varepsilon_3\delta_1\varepsilon_1\zeta_1\varepsilon_2]\delta\varepsilon\zeta\varepsilon_3\delta_1\varepsilon_1\zeta_1\varepsilon_2/\delta_1\varepsilon_3\zeta\varepsilon\delta\varepsilon_2\zeta_1\varepsilon_1[\delta_1\varepsilon_3\zeta\varepsilon\delta\varepsilon_2\zeta_1\varepsilon_1]\ldots . \quad (16)$$

The model (15) is shown as Fig. 9c. The model without Ge-atoms on the layer ζ_1 at the defect plane is given in Fig. 9c'. In Fig. 9d the model (16) is presented. Figures 9c and 9c' are symmetrical about the layer ζ_1 at the defect plane, and thus they are twin boundaries.

There are five possible defect structures, presented in Fig. 9a for the stacking (13), in Fig. 9b for (14), in Figs. 9c and 9c' for the stacking (15) and in Fig. 9d for (16). In order to find the best structure model, image contrasts for HREM were calculated and compared with the observations. Figure 10 presents the theoretically calculated images of the defect models shown in Fig. 9. Among the five figures, Figs. 10a and 10c' (which correspond to Figs. 9a and 9c') have the characteristic features of the corresponding observed image presented in Fig. 4a. The spots at the boundary are not weak, and their arrangements are symmetrical with respect to the defect plane. Assuming that the translation vector of the {100} defects is the same as the vector of the {110} defects when both defects are connected, Fig. 10c' must be selected as the relevant one. In conclusion, the twin boundary of the model Fig. 9c' with a translation of $\frac{1}{2} \cdot [111]$ is the best structure model to represent the observed electron microscopic contrast.

4.3. Characteristics of the Defect Structure

By comparing the observed and calculated images in chapters 4.1 and 4.2, the

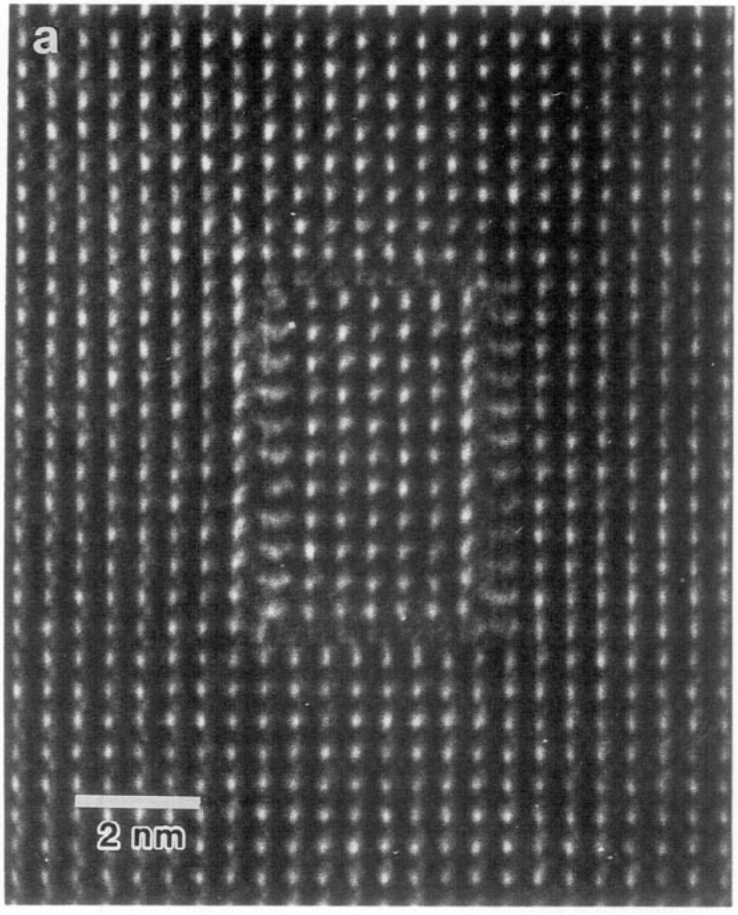

FIG. 12. Set of planar defects surrounding a prism observed along [001]. The periodicity of the image corresponds to the unit cell. (a) Without a dislocation. (b) and (c) With dislocations. The Burgers circuit surrounding the rectangular defect sets is shown; the Burgers vectors are drawn with small arrows.

translation vector has been determined as $\frac{1}{2} \cdot \langle 111 \rangle$ for the defects on the {100} and {110} planes (Fig. 11). The proposed models shown in Figs. 6c and 9c′ are the defect models considered earlier by Essmann and Zerweck (2). They are stacking faults along [100] and [110], respectively. In these models, chains of Nb atoms along [100] and/or [010] are disturbed. On the other hand, the arrangements of Ge atoms are conserved, although the Ge atoms at the defect plane are omitted in Fig. 9c′. The local atomic configurations around the defect planes are very closely related in these two models for the {100} defect (Fig. 6c) and for the {110} defect (Fig. 9c′). There are short interatomic distances at the defect, i.e., Nb–Nb (0.189 nm), in both models. Thus these atom positions should slightly deviate from the ideal ones. In conclusion, the existence of planar defects, whose structure models were considered earlier (2), were obviously confirmed by our experiments.

5. Defects in the Form of a Prism

Occasionally planar defects form rectangular shapes in the (001) projection. They

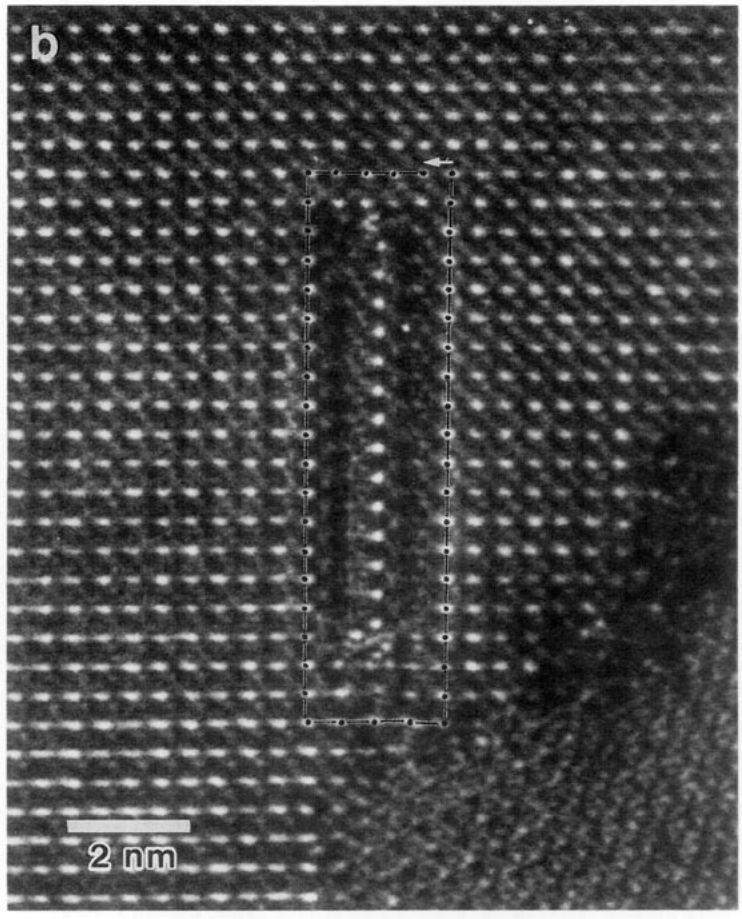

FIG. 12—*Continued*

must have the form of prism. Three examples of this type of defects are presented in Fig. 12. Figure 12a is the simplest example where the defect set does not require any other associated defects, e.g., dislocations. Since four {100} planar defects of Fig. 12a have the translation of $[\frac{1}{2}\,\frac{1}{2}]$ in this projection, their three-dimensional translation vector can be assumed to be $\frac{1}{2} \cdot \langle 111 \rangle$, which is the major translation of the {100} defect. A set of six planar defects in {100}, which have the translation of $\frac{1}{2} \cdot \langle 111 \rangle$, constituting an orthorhombic polyhedron, is also possible without any associated defects, although this has not yet been observed. In Fig. 12b the prism is near the grain boundary. Because of the stress at the boundary region, the prism is associated with a dislocation. The Burgers vectors of the dislocation may be of the $\langle 100 \rangle$ type. In Fig. 12c the prism is near the grain boundary and associated with a short planar defect in (110) as indicated by an arrow (length is about 3.6 nm). Because of the stress exerted by the grain boundary, the shift of the spot by this planar defect is not uniform along the defect. For this defect in (110), the observed translation in the image plane is [0.78 0.63] at the right upper part and [0.86 0.71] at the left lower part. Therefore the ideal translation of this defect may be $[\frac{3}{4}\,\frac{3}{4}]$ where two atom planes in (110) are missing. By this planar defect, a partial dislocation must be induced, since it ends inside a grain. The Burgers circuit

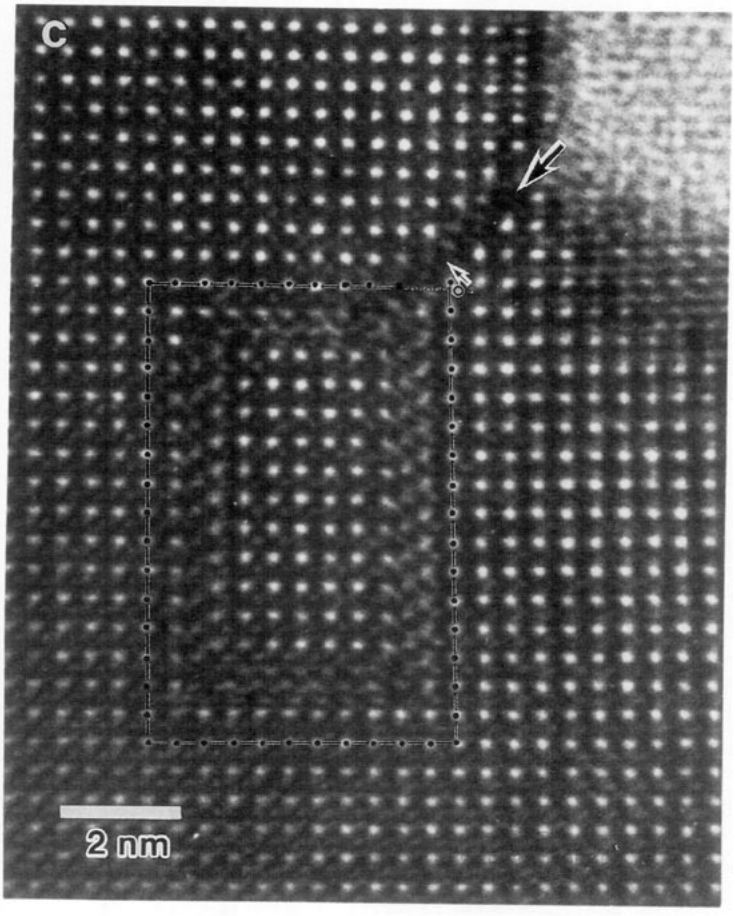

FIG. 12—*Continued*

surrounding the rectangular defect is shown superimposed in the image, whereby the probable spot position is extrapolated from the left part of the defect in (110). Translations of four defects in {100} defining the rectangular shape are $p \approx 0.39 \sim 0.44$ and $q = 0.47 \sim 0.49$, where p and q are translations perpendicular and parallel to the defect planes, respectively. Thus in this projection these translations are in principle $[\frac{1}{2}\ \frac{1}{2}]$. The deviation of the translation from the ideal value $\frac{1}{2}$ is due to the stress exerted by the grain boundary and possibly also to the partial dislocation induced by the planar defect in (110).

6. Summary and Conclusion

In the specimens investigated, planar defects of the Nb_3Ge structure occur mainly in {100} and {110} planes. By comparing the observed and the calculated images using probable structure models for the defects, the existence of $\frac{1}{2} \cdot \langle 111 \rangle$ stacking faults is experimentally confirmed by the present study. Since these planar defects frequently change their orientations, the fault energy of planar defects in {100} and {110} with the translation vector $\frac{1}{2} \cdot \langle 111 \rangle$ must have similar values. The planar defects described here are frequently observed in QTF-regions which contain a majority of small A15

TABLE I

CHANGES OF ATOMIC LAYERS ALONG [100] BY TRANSLATIONS (a) PARALLEL OR (b) PERPENDICULAR TO THE DEFECT PLANE (100), AND (c) THOSE ALONG [110]

(a)

Shift	α	β	γ
$\frac{1}{2}$ [010]	α_1	β_1	γ_1
$\frac{1}{2}$ [001]	α_2	β_2	γ_2
$\frac{1}{2}$ [011]	α_3	β_3	γ_3

(b)

Shift	α	β	γ
$\frac{1}{2}$ [100]	γ	β	α

(c)

Shift	δ	δ_1	ε	ε_1	ε_2	ε_3	ζ	ζ_1
$\frac{1}{2}$ [110]	δ_1	δ	ε_1	ε	ε_3	ε_2	ζ_1	ζ
$\frac{1}{2}$ [001]	$\delta_2 = \delta$	$\delta_3 = \delta_1$	ε_2	ε_3	ε	ε_1	$\zeta_2 = \zeta_1$	$\zeta_3 = \zeta$
$\frac{1}{2}$ [111]	$\delta_3 = \delta_1$	$\delta_2 = \delta$	ε_3	ε_2	ε_1	ε	$\zeta_3 = \zeta$	$\zeta_2 = \zeta_1$

grains, while they have rarely been observed in other regions of Nb–Ge films or in other A15 substances with mainly large grain sizes. This suggests that the frequent occurrence of the planar defects may be due to the influence of stress fields at the grain or phase boundaries associated with these defects. Therefore, the energy required to introduce such planar defects may be relatively high.

Acknowledgments

We are grateful to Professor T. Ishimasa and Mr. M. Stenzel for helpful discussions, to Mr. J. Reiner for the film preparation, and to Mr. R. Wessicken and Mr. P. Wägli for technical assistance. Financial support for M. A. by Schweizerische Volkswirtschaftsstiftung is gratefully acknowledged.

References

1. M. WEGER, *Rev. Mod. Phys.* **36,** 175 (1964).
2. U. ESSMANN AND G. ZERWECK, *Phys. Status Solidi b* **57,** 611 (1973).
3. Y. UZEL AND H. DIEPERS, *Z. Phys.* **258,** 126 (1973).
4. T. ISHIMASA AND Y. FUKANO, *Jpn. J. Appl. Phys.* **22,** 1092 (1983).
5. H. YOSHIDA, Y. HAYASHI, H. KODAKA, AND K. SHOJI, "Proc. Japan-US Workshop on High-Field Superconducting Materials for Fusion," p. 147 (1984).
6. H. YOSHIDA AND M. TAKEDA, *Annu. Rep. Res. Reactor Inst. Kyoto Univ.* **18,** 159 (1985).
7. Y. KITANO, H.-U. NISSEN, W. SCHAUER, AND D. YIN, "Proc. 17th Internat. Conf. Low Temp. Phys.," Part 1, p. 615, Karlsruhe (1984).
8. Y. KITANO, H.-U. NISSEN, R. WESSICKEN, D. YIN, AND W. SCHAUER, *J. Appl. Phys.* **58,** 1904 (1985).
9. M. STENZEL, Diploma thesis, Univ. Karlsruhe and Kernforschungszentrum Karlsruhe, Inst. für Tech. Phys., Karlsruhe, Germany (1985).
10. H.-U. NISSEN, Y. KITANO, AND R. WESSICKEN, *J. Microsc.* **142,** 171 (1986).
11. M. ARITA, Doctoral thesis, ETH Zürich, No. 8288 (1987).
12. D. YIN AND W. SCHAUER, KfK-Internal Report, 03.05.02 P01E, Kernforschungszentrum Karlsruhe, Karlsruhe, Germany (1982).
13. D. YIN, W. SCHAUER, AND F. WÜCHNER, *IEEE Trans. Magn.* **MAG19,** 276 (1983).
14. M. ARITA, H.-U. NISSEN, AND W. SCHAUER, *Phys. Status Solidi a* **88,** K1 (1985).
15. M. ARITA, H.-U. NISSEN, AND W. SCHAUER, *J. Solid State Chem.* **84,** 386 (1990).
16. A. J. SKARNULIS, E. S. VILLE, AND L. EYRING, *J. Solid State Chem.* **23,** 59 (1978).